

Stellar rotational periods in the planet hosting open cluster Praesepe

Géza Kovács^{1,2*}, Joel D. Hartman³, Gáspár Á. Bakos^{3,4}, Samuel N. Quinn^{6,7}, Kaloyan Penev³, David W. Latham⁵, Waqas Bhatti³, Zoltán Csubry³ and Miguel de Val-Borro³

¹*Konkoly Observatory, Budapest, Konkoly Thege M. u. 15-17, Hungary*

²*Department of Physics & Astrophysics, University of North Dakota, 101 Cornell Street, Grand Forks, ND 58202, USA*

³*Department of Astrophysical Sciences, Princeton University, Princeton, NJ 08544, USA*

⁴*Sloan Fellow*

⁵*Harvard-Smithsonian Center for Astrophysics, 60 Garden Street, Cambridge, MA 02138, USA*

⁶*Department of Physics & Astronomy, Georgia State University, 25 Park Place NE Suite 605, Atlanta, GA 30303*

⁷*NSF Graduate Research Fellow*

Submitted/Accepted April 3, 2014/May 9, 2014

ABSTRACT

By using the dense coverage of the extrasolar planet survey project HATNet, we Fourier analyze 381 high-probability members of the nearby open cluster Praesepe (Beehive/M44/NGC 2632). In addition to the detection of 10 variables (of δ Scuti and other types), we identify 180 rotational variables (including the two known planet hosts). This sample increases the number of known rotational variables in this cluster for spectral classes earlier than M by more than a factor of three. These stars closely follow a color/magnitude – period relation from early F to late K stars. We approximate this relation by polynomials for an easier reference to the rotational characteristics in different colors. The total (peak-to-peak) amplitudes of the large majority (94%) of these variables span the range of 0.005 to 0.04 mag. The periods cover a range from 2.5 to 15 days. These data strongly confirm that Praesepe and the Hyades have the same gyrochronological ages. Regarding the two planet hosts, Pr0211 (the one with the shorter orbital period) has a rotational period that is ~ 2 days shorter than the one expected from the main rotational pattern in this cluster. This, together with other examples discussed in the paper, may hint that star-planet interaction via tidal dissipation can be significant in some cases in the rotational evolution of stars hosting Hot Jupiters.

Key words: open clusters and associations: individual (Praesepe, M44, NGC 2632) – planetary systems – stars: rotation – stars: starspots – variables: δ Scuti

1 INTRODUCTION

The well-known significance of open clusters in studying stellar evolution and various aspects of galactic structure and cosmic distance calibration has been highlighted recently by the analysis of the photometric databases collected by both target-oriented projects, such as the MONITOR project (e.g., Irwin et al. 2009) and by the ground- and space-based surveys of transiting extrasolar planets (TEPs). It is important to note that before these surveys and special projects, the data on rotational variables (i.e., on spotted

stars with measurable photometric variability) were fairly scarce. For example, the first few variables of this type were discovered in the otherwise well-known nearby cluster Praesepe only in 2007 (Scholz & Eislöffel 2007). The TEP surveys are very powerful means to discover variables, since they stare on the same large area of the sky for a period of three to six months (or longer) and gather good quality time series on 10^4 – 10^5 stars in their large field of views. As a ‘by-product’ of these surveys, several open clusters were caught and analyzed in searching for TEPs and other variables, including spotted stars (Pepper et al. (2008), [Praesepe]; Collier et al. (2009), [Coma Berenices]; Hartman et al. (2010), [Pleiades]; Delorme et al. (2011),

* E-mail: kovacs@konkoly.hu

[Hyades, Praesepe]; Cargile et al. (2013) [Blanco 1]). These latter types of variables play a crucial role in studying stellar rotation and its dependence on cluster age and stellar type. For a very recent review of this field we refer to Bouvier et al. (2013).

Earlier studies on stellar rotation via photometric variability were limited due to the sporadic nature of the observational campaigns and their focusing mostly on individual targets. Furthermore, main sequence stellar rotational periods are in the range of few to 10–20 days, which is not a comfortable range in following up low-amplitude variables with sparsely sampled ground-based observations. In addition, spot evolution and differential rotation lead to non-stationary frequency spectra, that may result in an inaccurate determination of the rotational periods, and in general, misinterpretation of the data. This is why previous works (before the era of TEP searches) were mostly limited to rotation effects producing signals above ~ 0.01 mag (e.g., Messina & Guinan 2002). Even though most of the wide-field ground-based surveys are carried out from a single site, and thus have daily gaps in their observations, they are still capable of detecting rotation signals with amplitudes in the *sub-mmag* regime, thereby unveiling the rotation properties of stars with spot sizes similar to those on the Sun. This sensitivity results from the dense sampling, long time coverage, and relatively high photometric precision per observation achieved by these surveys (typical values are: cadences of a few minutes, 10^3 – 10^4 total data points per star, and 0.01–0.02 mag accuracy per data point). This dramatically increases the number of stars, from spectral types M to A, for which stellar rotational periods may be measured, and allows a deep analysis of angular momentum loss and stellar evolution.

From the point of view of extrasolar planets, open clusters are also important in addressing questions on the role of stellar environment in the early phases of planetary system evolution. Although considerable efforts have been made over the past to find planets in clusters using both spectroscopic (i.e., radial velocity) and photometric (i.e., transit) methods, these searches did not bear fruits until fairly recently. As of this paper, we know 11 planets in six open clusters. We have three long period ($P > 600$ days) radial velocity planets in the Hyades, NGC 2423 and NGC 4349 (Lovis & Mayor 2007; Sato et al. 2007). The other eight systems have shorter periods. There are two radial velocity planets in Praesepe ($P = 4.43$ and 2.15 days, Quinn et al. 2012), one in the Hyades ($P = 6.09$ days, Quinn et al. 2014), three in M67 ($P = 6.96$, 5.12 and 121.71 days, Brucalassi et al. 2014) and two TEPs from the Kepler satellite in NGC 6811 ($P = 15.73$ and 17.82 days, Meibom et al. 2013). Although this sample is still small, the number of planets hosted by cluster stars seems to be in agreement with those derived from field stars (this is true both for Hot Jupiters and for (sub)Neptunes – see Quinn et al. 2014 and Meibom et al. 2013, respectively).

Since the ages and the chemical compositions of the open clusters above are much more accurately known, than, in general, those of the field stars, with the five Hot Jupiters (HJs) residing in Praesepe, Hyades and M67, one can start addressing several questions (such as planet formation, migration and star-planet interaction) in a more efficient way. In particular, because of the usually well-defined rotational

pattern of cluster stars, one may ask if tidal interaction between the planet and the star can lead to the spin-up of the host star (Brown et al. 2011; Penev et al. 2012; Zhang & Penev 2014). The difference between the rotational periods of single and planet host stars yields an important constraint on the tidal dissipation factors Q_{star} and Q_{planet} . There are only bulk estimates on these parameters, although they are crucial in any tide-related problems (e.g., they scale the circularization and in-spiral times for close-in planets).

Using photometric time series observations from the HATNet¹ project, here we derive rotational periods for 180 K to F stars in Praesepe (M44/NGC 2632/Beehive). We use the tight period–color (also period–luminosity, or period–mass) relation spanned by these data to investigate the possibility of orbital momentum transfer in the two systems containing HJs. The results are compared with the Hyades, another planet hosting cluster, similar to Praesepe.

2 FREQUENCY ANALYSIS OF THE CLUSTER MEMBERS

2.1 The HATnet data coverage

In selecting cluster members we rely on the membership analysis of Kraus & Hillenbrand (2007), based on various archival color, magnitude and proper motion data. In their Table 3 there are 1130 stars listed as candidate cluster members, an overwhelming majority of which have large membership probabilities. Here we match all of them with the HATNet database and find that there are altogether 408 objects that match within $0.22''$ of a HAT target (based on the 2MASS catalog). The remaining stars in the membership catalog yield much larger matching distances (greater than $9''$). This is because they have faint magnitudes and, as a result, they are absent from the HATNet database. Therefore, we have many inaccurate object identifications among the fainter stars with associated bad matching distances. This results in a poor sampling of the M dwarf regime, and, consequently, no coverage of the cooler M stars, where magnetic braking is not yet effective and the rotational periods have significant scatter due to the different initial conditions with which stars started their lives in the interstellar cloud. Although we have poor sampling in the M star regime, the HATNet survey is able to reach fast rotators at the blue end, which is also important, since this part of the diagram is still poorly known, largely due to the lower amplitudes of these variables. From the 408 targets we omit 27 which have

¹ The Hungarian-made Automated Telescope Network (Bakos et al. 2004) consists of 6 wide field of view, small-aperture autonomous telescopes located in Hawaii (Mauna Kea) and Arizona (Fred Lawrence Whipple Observatory). The prime purpose of the project is to search for extrasolar planets via transit technique.

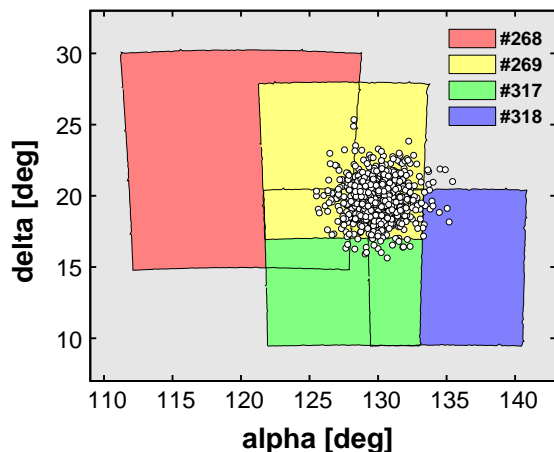


Figure 1. Coverage of Praesepe by the HATNet fields. The 1130 candidate members given by Kraus & Hillenbrand (2007) are shown as open circles.

a small number of data points² and we end up with a sample of 381 stars as the basic set for the frequency analysis.³

Praesepe has a very fortunate position in respect of the distribution of the HATNet fields. The cluster sits in the overlap area of four fields (see Fig. 1), yielding long-timebase coverage with high number of data points for most of the stars. Although there are four fields, their relative positions are such that cluster members may have only up to three-fold coverage. Further details of the field-wise data distribution are given in Table 1. The longest and most abundant coverage comes from the overlaps of fields #269, 317 and 318 with the total time span and datapoint number of 917 days and 14400, respectively. The integration time is 3 min for all fields, except for #318, for which we used 5 min integrations. With the read-outs and data storage, the sampling times are $\sim 20\%$ longer than these integration times. All observations were taken through the Sloan r filter.

The distribution of the cluster member candidates of Kraus & Hillenbrand (2007) on the color-magnitude diagram (CMD) is shown in Fig. 2. The lighter/blue shade/color denotes the 408 HATNet matches, including the two radial velocity (RV) planet hosts. This sample extends from early F to late K stars and follows a fairly well-defined isochrone corresponding to $[\text{Fe}/\text{H}] = 0.11$ and age of 590 Myr (Khalaj & Baumgardt 2013, see however Gaspar et al. 2009 for a possible higher age of 757 Myr). A particular property of the CMD is the distinct high-luminosity branch between F- and early M-type stars. The common explanation of this branch is that these stars are either blended by some neighbors in the denser inner part of the cluster, or they are binaries with luminous secondary components (see, e.g., Khalaj & Baumgardt 2013, Wang et al. 2014). However, we note that an alternative explanation, involving an earlier

² We set the limit to 1000 data points, mainly because when applying systematics filtering (TFA, see Sect. 2.2 and Kovács et al. 2005) we use a large number of templates; stars have different number of data points depending on their brightnesses and positions on the sky.

³ The light curves of these stars are deposited at the Strasbourg astronomical Data Center: <http://cdsweb.u-strasbg.fr/>

Table 1. HATNet fields covering Praesepe.

Field	JD _{first}	JD _{last}	T [days]	N _{dp}	N _{clus} ^{all}	N _{clus} ^{act}
268	55873	56070	197	7750	29	2
269	55674	55728	54	2750	403	374
317	55507	55672	165	8400	337	315
318	54811	54964	153	2900	278	241

Notes: JD_{first}, JD_{last} (minus 2400000), T (total time span) and N_{dp} (number of data points) may change from object to object. The values listed are average values. N_{clus}^{all}: all overlaps with the cluster member list of Kraus & Hillenbrand (2007); N_{clus}^{act}: actual (N_{dp} > 1000) overlaps with the list mentioned. Because the same object may appear in up to three fields, the total number of HATNet objects with cluster-membership and available light curve is only 381.

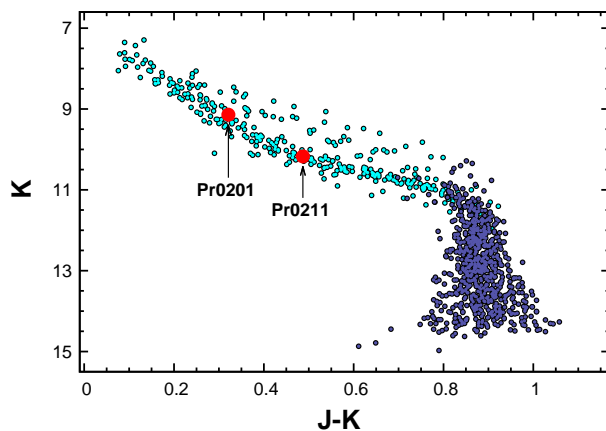


Figure 2. Color-magnitude diagram of Praesepe with the two planet host stars highlighted by larger filled circles. The 1130 cluster candidates as given by Kraus & Hillenbrand (2007) are plotted in the 2MASS color system. The 408 matching objects with the HATNet database are shown by light-shaded points.

mixing with another stellar population of different age may also be viable (Franciosi et al. 2003). It is also seen that the two planet hosts fit well to the densely-populated main sequence with no apparent second luminous components.

2.2 Pre-analysis data conditioning

Since our time series preparation methods were developed in the context of transiting extrasolar planet search, we think it is useful to briefly describe the main aspects of our approach. For additional details on the two methods summarized below we refer to Kovács et al. (2005) and Bakos et al. (2010).

We use External Parameter Decorrelation (EPD) and Trend Filtering Algorithm (TFA) to clean up the data from systematics before the frequency analysis. These are crucial steps, since we usually deal with small-amplitude signals, that are either completely buried in the systematics or seriously crippled by them.

The idea of the EPD filtering is based on the observation that certain external parameters $\{p_i\}$ of the stellar image (such as PSF width, elongation, chip position, hour angle, color, etc.) correlate with ΔF , which is the

residual stellar flux after subtracting off the median of the signal. The functional form of $\Delta F(p_1, p_2, \dots)$ is determined numerically through a fit of $\{p_i\}$ to ΔF by using all individual flux measurements for each selected star. The correlation is determined for each star separately. Therefore, while the functional form of the correlation is the same, the regression coefficients will differ for each individual star. Once the correction function is found, it is employed on each star on each flux value individually by $F_{\text{corr}}(t) = F_{\text{in}}(t) - \Delta F(p_1(t), p_2(t), \dots)$, where $F_{\text{in}}(t)$ is the incoming flux and $\{p_i(t)\}$ are the time-dependent external parameters. We note that although this step contains only the subtraction of a pre-determined function evaluated at the temporal values of the EPD parameters and stellar flux measurements, the regression is obtained by a fit to the target time series, and, as a result, the underlying signal might also be affected by this process. Our experience shows that this effect is usually small, and can be corrected at a later step with full time series model fitting (see Bakos et al. 2010).

TFA has a different philosophy in finding systematics in photometric time series. Akin in part to the traditional ensemble photometry, it is assumed that systematics exhibit themselves in many objects in a similar manner. In the case of standard ensemble photometry this behavior is simply utilized by calculating the average flux of a large number of neighboring stars and dividing the flux of the target by this average. However, in the case of TFA we assume that not all stars have the same systematics but for any given target we can find a time series $\{Z(t_i)\}$ that is optimum in terms of systematics (i.e., it contains most of them, characteristic for the target signal). The optimization is achieved by using the time series of m number of comparison stars (or templates) $\{C_j(t_i)\}$ and searching for the optimum filter $\{U(t_i)\}$ in the form of the linear combination of these template time series: $U(t_i) = \sum_{j=1}^m a_j C_j(t_i)$. The regression coefficients $\{a_j\}$ can be found, e.g., by fitting $\{U(t_i)\}$ to $\{Z(t_i)\}$ by least squares. The filtered time series is obtained by subtracting $\{U(t_i)\}$ from $\{Z(t_i)\}$. In this process we assume that the target time series is dominated by systematics - the non-reconstructive application of TFA. This assumption can be lifted once a signal is found, and a complete model is fitted that includes also the signal - the reconstructive application of TFA).

2.3 Frequency analysis

We employ the method of standard Discrete Fourier Transformation (DFT, Deeming 1975) to search for significant close-to-sinusoidal signals in the above dataset of 381 light curves (LCs). The analysis is performed both on the basic product of the HATNet pipeline, comprising the time series after EPD and on the TFA-filtered time series of the EPD data. When analyzing the EPD data, we merge the LCs from the individual fields by shifting their averages to the same level. For the TFA-filtered data we perform non-reconstructive TFA filtering for each field separately, and then we merge the so-obtained LCs in the same way as we do for the EPD data. The analyses of the two types of datasets are complementary. The EPD data still contain various systematics, thereby weakening our ability to detect faint signals. On the other hand, application of TFA-filtering might

lead to losing some of the variables due to over filtering, especially if they are on the longer period side and if there are other stars in the field with similar periods. Although our earlier works on different datasets (Szulágyi et al. 2009; Dékány & Kovács 2009) showed that the chance of this to happen is reasonably low, incorporating the original (EPD) data may further reduce the likelihood of this event. Furthermore, because several/many rotational variables in a cluster exhibit very similar periods, to minimize the effect of ‘squeezing’ the amplitudes when TFA is employed, we iteratively deselect suspected variables from the TFA templates.

In the variability search we test narrow-, medium- and high-frequency bands for the EPD and the TFA-filtered data. For the latter, we use 600 templates selected as mentioned above. For the frequency bands we choose the ranges of $[0, 0.5]\text{d}^{-1}$, $[0, 10]\text{d}^{-1}$ and $[10, 50]\text{d}^{-1}$. Both the frequency spectra and the folded LCs are examined. At the end of this process we conclude with 180 rotational and 10, mostly δ Scuti-type variables. The latter ones are summarized in the Appendix, whereas the rotational variables (including the selection procedure) are discussed in the subsequent sections.

3 ROTATIONAL VARIABLES

One of the distinct properties of main sequence cluster stars is that their rotational rates quickly (within a few hundred Myrs) settle down to a fairly tight sequence, usually parameterized by their mass, or by some other, observationally more easily accessible parameters, such as their colors (Barnes 2003). Therefore, unlike in the case of rotating (i.e., spotted) variables in the field, they are much easier to recognize, especially if the cluster is rich, older than ~ 100 Myr and the underlying photometric data are accurate and extended enough to detect (quasi)periodic variation down to the mmag level.

As an example of the striking appearance of rotational variables, in Fig. 3 we show all derived frequencies in the $r(\text{jhk})$ -frequency plane. The analysis covers the $[0, 2]\text{d}^{-1}$ range and includes a single pre-whitening step for each star (i.e., we plot two frequency values for each of the 381 stars: the peak frequencies obtained from the original and the pre-whitened data). The color coding for the signal-to-noise ratio (SNR) helps to recognize more easily the various ridges related to the main rotational sequence. The magnitudes in the Sloan r band are approximated by the following combination of the 2MASS colors (based on our linear regression to 410 stars of Stetson 2000 with colors covering the range relevant for Praesepe)⁴ for Fig. 3, we decided to use exclusively these approximate Sloan r magnitudes, instead of mixing the two sets. In all other cases either the APASS or the 2MASS magnitudes are employed. We avoid using HATNet instrumental ‘ r ’ magnitudes, since the HATNet magnitudes are often unreliable, due to the limited spatial resolution of the images.

$$r(\text{jhk}) = 0.6975 + 2.9782J - 0.8809H - 1.1230K \quad (1)$$

⁴ Because of the several non-matching objects with the APASS database (<http://www.aavso.org/apass>)

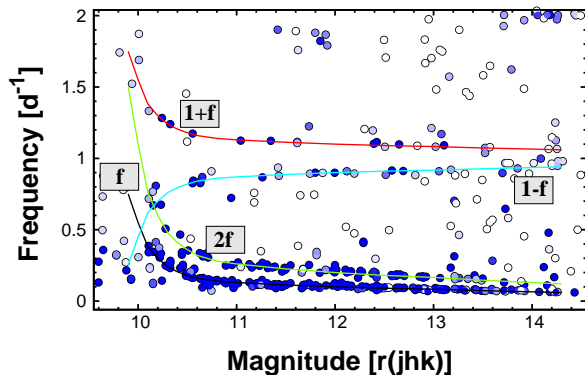


Figure 3. Frequency versus approximate Sloan r (jhk) magnitudes for our Praesepe sample. All frequencies found as the highest peaks in the frequency spectra of the data and in their residuals after the first pre-whitening are plotted (i.e., two points for each star). The points are color/shade-coded from high signal-to-noise ratio ($\text{SNR} > 8$, dark) to the low one ($\text{SNR} < 5$, white). The analysis was made in the $[0, 2] \text{ d}^{-1}$ frequency band. The derived rotation line (see text) is used to show the various frequency patterns due to aliases and confusion with harmonic components.

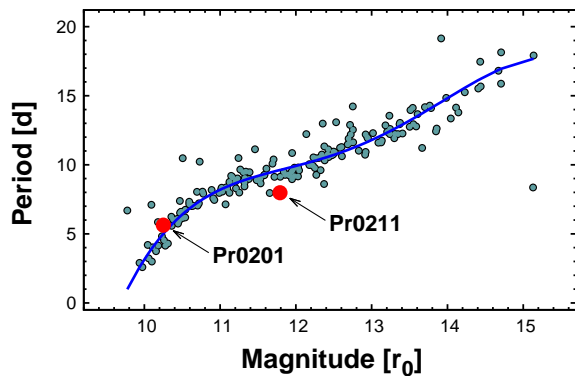


Figure 4. Dereddened Sloan r magnitudes versus period for our rotational variable star sample of 180 stars in Praesepe (see Table 2). The continuous line is a 4th-order polynomial fit to the data (see Table 3). The two RV planet hosts of Quinn et al. (2012) are shown by the larger filled circles.

The rotational sequence (labelled by the letter ‘f’) shows up very clearly, as does the one related to the 1st harmonic (sequence ‘2f’). Other components, due to 1 d^{-1} aliasing (sequences ‘ $1 \pm f$ ’) show up too, albeit with a sparser population, indicating that in most cases aliasing is not an issue in the available dataset.

After the identification of the main rotational ridge, we go through the multistep variability check as described in Sect. 2.3 and construct the final rotational ridge by correcting the peak frequencies, if they belong to some of the secondary ridges mentioned above. Here we extend the correction due to harmonic components up to the 4th harmonic – because of the degeneracy between the observed and the rotational periods we may need to consider also these, more

involved cases.⁵ In constructing the ridge, we iteratively develop the average ridge line, which is a 4th-order polynomial fit to the data. In deciding whether a frequency value should or should not be corrected for harmonics or aliases, we consider the difference between this frequency point and the one corresponding to the ridge value (at the given r magnitude). The consecutive steps in the frequency correction and polynomial fitting constitutes the iterative process.

After multiple screenings of all the stars analyzed, we end up with 180 rotational variables (see Table 2). The positions of these stars on the r [mag]–period plane are shown in Fig. 4. We see that indeed, the relation is fairly tight, although there are some 13 outliers (arbitrarily defined as those with relative distances from the ridge greater than 20 % – i.e., $|\nu/\nu_{\text{ridge}} - 1| > 0.2$). Except perhaps for a few low-SNR variables, all are very secure detections. None of them have other frequencies in the $[0, 50] \text{ d}^{-1}$ band (except for possible harmonic components). Some of them at the fainter (redder) end may well belong to the group of stars that have not yet converged to a tight rotational sequence. An additional source of ambiguity in this diagram is the reliability of the associated magnitude/color values. These might be strongly affected by blending in the more crowded region of the cluster. We also mention that except for two (HAT-269-0000761 and HAT-269-0000794) of the 24 spectroscopic binaries common with the list of Mermilliod et al. (2009), all follow the overall r [mag]–period relation shown in Fig. 4.

It is important to note that we also detected the rotation of the two planet hosts. The ratios of the orbital to the rotational periods are non-commensurate in both systems. For Pr0201=HAT-269-0000805 $P_{\text{orb}}/P_{\text{rot}} = 0.787$ whereas for Pr0211=HAT-269-0002316 this ratio is 0.270. This further supports the planetary nature of these systems, since the periods of the radial velocity signals are not integer multiples/fractions of the rotational periods as one might expect if the radial velocity variations were caused by stellar activity.

In comparison with similar plots from other clusters, it is seen that we miss the faint end of the progression, where the lack of magnetic braking shows up as a suddenly increased scatter in the periods. Our survey (similarly to that of Delorme et al. 2011) is too shallow to cover this rather faint magnitude range. However, the PTF project covered just this range for this cluster, and, indeed, found 40 variables with a wide period range of 0.5 to 36 days (Agüeros et al. 2011). Similarly, the deep survey by Scholz et al. (2011) resulted in the discovery of 26 fast rotating ($P_{\text{rot}} < 2.5 \text{ d}$) objects in the very low ($M < 0.3M_{\odot}$) mass regime. The recent analysis by McQuillan, Aigrain & Mazeh (2013) confirms this wide period distribution also for the Kepler field M stars. Toward the blue end, on the other hand, due to the field overlaps, our survey is sensitive to periodic variations down to a few mmag. This leads to a good coverage of the progression in this regime, where the roughly linear color dependence becomes nonlinear and the rotational

⁵ A simple example of this degeneracy is when two spots of equal size are at the same latitude but at opposite longitudes. The resulting photometric signal will have a period of half that of the rotational period.

Table 3. Polynomial fits to the ridge values.

color	a_0	a_1	a_2	a_3	a_4	cmin	cmax
V	10.724	4.356	3.011	3.240	-3.942	9.941	15.787
B-V	11.528	4.934	1.277	1.446	-2.897	0.483	1.714
r	10.006	3.132	1.147	3.483	-2.233	9.906	14.218
K	9.579	4.633	-0.755	4.083	0.000	8.580	11.505
J-H	10.380	3.917	-0.240	2.096	0.000	0.180	0.722
J-K	10.447	2.975	0.675	4.020	0.000	0.247	0.903

Notes: See Eq. (2) and the subsequent explanation for the use of the data in this table. By omitting outliers at the 3σ level, the above regressions fit the 180 rotational variables with standard deviations of 0.7, 0.9, 0.7, 1.0, 1.2 and 1.2 days for V, B-V, r, K, J-H and J-K, respectively. The number of the corresponding outliers are 11, 7, 11, 8, 5 and 3.

planet hosts to the overall rotational patterns in different clusters.

For an easier reference to the ridge values in the various colors, we fit m -th order polynomials to the respective color-period relations

$$P = \sum_{i=1}^{m+1} a_{i-1} x^{i-1}, \quad (2)$$

where $x = k(c - \langle c \rangle)$, $k = 2/(c_{\max} - c_{\min})$, $\langle c \rangle = (c_{\max} + c_{\min})/2$ and c_{\min} , c_{\max} , respectively, refer to the (min,max) values of the given dereddened color ‘ c ’ in the region we fit the periods. Dereddening is performed with $E(B - V) = 0.027$ and standard relative reddening coefficients (e.g., Yuan et al. 2013). For V, B-V and Sloan r the order of the polynomial (m) is equal to 4, whereas for the 2MASS colors we choose $m = 3$, because of the lower stability of the fit for these colors at higher polynomial orders. In finding the best fit to the ridge, we employ sigma clipping at the level of 2.5σ . The resulting coefficients are listed in Table 3.

3.1 Compatibility with the observed rotational velocities

If spectroscopic $V_{\text{rot}} \sin i$ values are available, it is customary to compare these values with the derived rotational periods. We use the data from the spectroscopic survey of open clusters by Mermilliod et al. (2009). By cross-correlating the data published for Praesepe with our rotational variable list, we find 88 matches. These stars are plotted in Fig. 5. For the computation of the expected rotational rates we estimate the radii of the stars by using the Padova isochrones⁶ for the age of 590 Myr with solar-scaled composition at $Z = 0.02$. For the overall cluster reddening we set $E(B - V) = 0.027$ mag and for the distance modulus we use 6.30 mag. These values are taken from Fossati et al. (2008), Boesgaard & Roper (2013), Taylor (2006) and van Leeuwen (2009) and are in the overall ranges of the most frequently quoted parameters for this cluster.

Although the isochrone corresponding to the above parameters fits the $(J - K, K)$ diagram quite well in the $J - K$ regime between 0.2 and 0.8, it fails to reproduce the break at

⁶ see Bressan et al. (2012) and <http://stev.oapd.inaf.it/cmd>

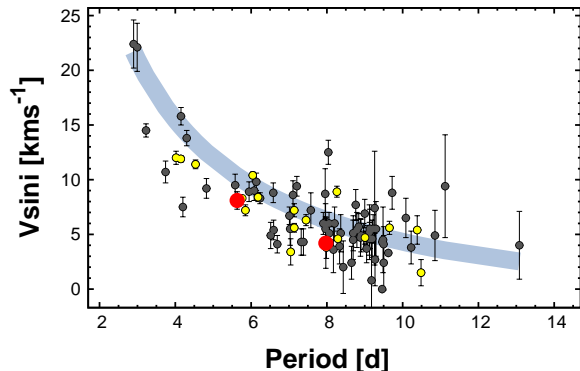


Figure 5. Photometric periods versus observed rotational velocities by Mermilliod et al. (2009) for the objects in common with our list of rotational variables (see Table 2). The RV planet hosts are shown by the bigger filled circles, the spectroscopic binaries from Mermilliod et al. (2009) by the ones with lighter shade. The thick continuous line is drawn by using Eq. (3). The line covers the stellar rotational velocities derived from the observed rotational periods and stellar radii given by model isochrones.

$J - K \sim 0.85$. As discussed by Khalaj & Baumgardt (2013), other isochrones fit this particular part better but are less successful in reproducing the hotter part of the main sequence. Since we are focusing on stars between A and M spectral types, and our experiments with other isochrones led to similar results to those of the Padova isochrones, we decided to use these latter ones in the estimation of the stellar radii. We found that the computed stellar rotational velocities can be well fitted by the following simple formula

$$V_{\text{rot}} = 57.0 P_{\text{rot}}^{-(1.0+0.03(P_{\text{rot}}-6.0))}, \quad (3)$$

where P_{rot} is the measured rotational period (in [days]). The thickness of the line shown in Fig. 5 covers the range of scatter due to observational errors in the 2MASS colors. It is important to note that the above formula can be employed only on this cluster, since it depends on the age and chemical composition, specific to this cluster.

We think that the agreement between the observed and expected rotational velocities is reasonably good. For ideal (errorless) observed rotational velocities we should see the ‘theoretical’ equatorial velocities (thick gray line in Fig. 5) as the upper envelope of the observed values. We see that some stars are above this line. Several of them have reasonably large error bars to consider their outlier status insignificant, but some of them may pose some concern, such as HAT-269-0001124 at the period of 8.04 d with small error and well-established period.

3.2 Color – amplitude dependence

It is important to investigate if the amplitude of the observed variability has any tendency of a correlated variation with some other properties of the star. Such a correlation might be expected from the underlying dependence of stellar activity on the same parameters (e.g., Mamajek & Hillenbrand 2008). Because the observed photometric amplitude is a multivariable function of the complicated physical processes (ro-

tation, local and global magnetic field variations, convection, turbulence, etc.) involved in the spot generation and also of the specific geometric configuration, we expect rather fuzzy relations between the amplitudes and some other observable parameters. Indeed, results published so far show that the relation is fairly vague, especially if we are aimed at a more comprehensive analysis (see Saar et al. 2011 for a step in this direction).

To add further piece of information to this issue, by using the data of Table 2, we show the variation of the peak-to-peak amplitudes as a function of $(J - K)_0$ in Fig. 6. The dependence is similar to most of the published results; redder (fainter, longer-period) stars tend to have larger amplitudes. We note that employing the Rossby number (the ratio of the rotation period to the convective turnover time – see Noyes et al. 1984), advocated by some studies (e.g., Hartman et al. 2009, Walkowicz & Basri 2013), yields also consonant result with similar scatter. Because of the data are more noisy and may contain less data points at the red (faint) end, we must address the question if the observed trend is the result of noise-limited sampling. By using the simple assumption of Gaussian white noise, the Fourier amplitudes follow a frequency-independent χ distributions, therefore we can compute the average expected Fourier amplitude as $\langle A_{\text{noise}} \rangle = \sqrt{\pi/N}\sigma$. Here N is the number of data points and σ is the (assumed to be) uniform point-by-point standard deviation of the data. We estimate the expected signal amplitudes at the detection level of $k\sigma$ as $k < A_{\text{noise}} \rangle$. It is seen that the higher significance lower limits (black dots) nicely follow the lower boundary of the amplitudes of the detected variables. The lower significance lower limits (gray dots) show the same trend but rendering the suspected trend significant. Considering that our assumption on the noise properties is a gross simplification of the real data setting with gaps, systematics and associated colored noise, we incline to conclude that most of the observed trend comes from the lower signal detection efficiency at the high-noise end. The similarity of the trend of the statistical limit to that of the lower boundary of the variables also supports this conjecture.

3.3 The four types of variability

One particular problem with the photometric identification of the rotating variables is that the corresponding time series are non-stationary due to the finite life time and migration of the spots to different latitudes, where differential rotation leads to a frequency drift in the observed signal. In spite of this, it is expected that some level of coherence prevails and leads to a broad, but still well-defined peak in the frequency spectrum.

Although the peak profiles can supply valuable information on spot life times and migration/differential rotation, the current data are still not suitable for this kind of deep analysis, due to the interfering noise and gaps in the sampling. Nevertheless, some basic properties are easy to recognize and one can classify the observed frequency spectra based on these simple characteristics. Although this classification is phenomenological in nature, it adds further solid information to the occurrence rates of the most common types of rotation-induced variability.

Upon examining the frequency spectra (with some rep-

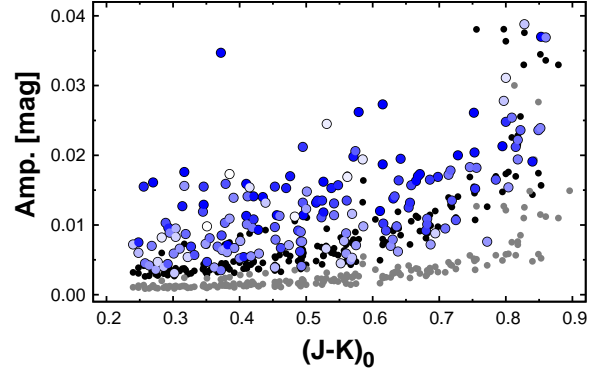


Figure 6. Variation of the peak-to-peak amplitudes (see Table 2) as a function of the 2MASS $(J - K)_0$ color (large shaded circles, with shading code from $SNR \leq 4$ [white] to $SNR \geq 14$ [deep blue/gray]). For reference, the 5 and 15 σ limits of signal detection (assuming white noise) are also shown on a star-by-star basis by gray and black filled circles, respectively. In order to scale the figure to the bulk of the sample, we left out a handful of stars with amplitudes larger than 0.04 mag. The apparent trend in the amplitudes is most likely associated with the higher detection limit toward redder colors (i.e., fainter stars).

resentative examples shown in Fig. 7), we find that all 180 stars classified as rotational variables fall in one of the following categories.⁷

(a) These variables apparently have monophasic sinusoidal light variation (i.e., no residual power left near the main peak after pre-whitening). We have 23 such cases in the present sample, which constitutes 13% of the rotating variables.

(b) There are 71 variables (i.e., 39% of the full sample) with a single but unstable sinusoidal component. Because of the frequency/amplitude drifts, these variables have inherently non-discrete Fourier spectra. Therefore, they show residual power close to the peak frequency even after several pre-whitening cycles (based on the piece by piece signal removal, assuming stationarity for each component).

(c) In 13 infrequent cases we can observe two peaks separated by a few times of the overall line width (i.e., by $\Delta\nu = 1/220\text{d}^{-1}$, where the basic time span of 220 days is determined by the compact/ \sim continuous time base of two of our fields, #269 and 317). The frequency distances are between $\sim 0.007\text{d}^{-1}$ and $\sim 0.020\text{d}^{-1}$ (with the exception of HAT-270-0000714, that has frequency components separated by $\sim 0.032\text{d}^{-1}$). The most common explanation of these separate components is that they are associated with the different latitudes of the stellar surface, that, due to differential rotation, carry the respective spots with different periods. We note that even the largest frequency separation

⁷ In addition to the possibility of overlapping properties, as always, there is the issue of noise. This may shift the actual statistics, depending on where the level of significance is set (which may be an issue here, since the noise is usually colored, leading to frequency-dependent detection significance). Here we try to avoid any dubious cases and rely on well-established detections.

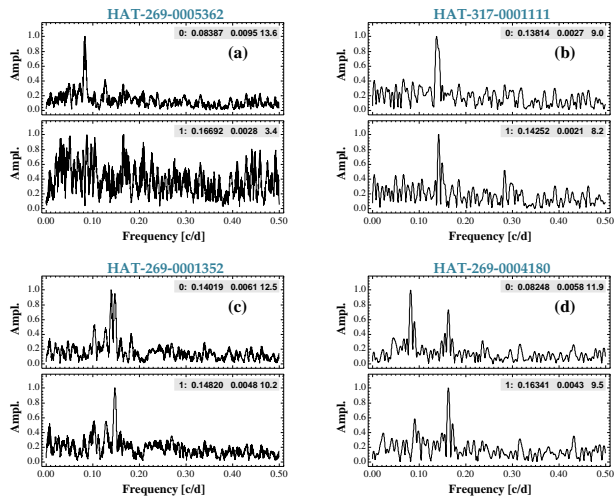


Figure 7. Examples for the four types of frequency spectra of the rotational variables as discussed in Sect. 3.3. In each sub-figure the upper and lower panels show, respectively, the frequency spectra of the data and the spectra obtained after the first pre-whitening (with the peak frequency shown on the upper panel). The insets display the pre-whitening order, the peak frequency, the amplitude and the SNR of the peak. The spectra are normalized to the highest peak in each panel.

is allowed by current models of differential rotation (e.g., Kitchatinov & Olemskoy 2012). These 13 stars constitute 7% of the full sample.

(d) As already indicated in Fig. 3, most of the frequencies with sufficient significance that do not sit on the main rotational ridge in the color/magnitude – period plot belong to the first harmonic of the rotational frequency. The first harmonic may have larger or smaller amplitude than that of the rotational frequency. There are altogether 73 stars (i.e., 41% of the sample) that have residual power either at the corresponding 1st harmonic or at a sub-harmonic frequency. The effect of the harmonics may show up either as a non-sinusoidal distortion or as a double hump in the light curve, indicating more complicated spot distribution in the latter case.

It maybe useful to investigate how the above type of formal classification relates to other parameters, in particular to the magnitudes or colors. In Fig. 8 we plot the above classes separately in the $r_0 - P$ plane. Interestingly, not all types of variables are distributed evenly in this plane. Although the particular distributions are related to the types with relatively low number of members, we think that for type (c) (variables with two closely spaced frequencies) and maybe also for type (a) (those with constant amplitude sinusoidal variations) we may state that they are preferably found at high and low/mid luminosities, respectively. Although we cannot offer an explanation for this distribution pattern at this moment, it is important to note that for short rotation periods (i.e., higher luminosities) differential rotation results in a larger difference in the rotational periods between the pole and the equator (e.g., Kitchatinov & Olemskoy 2012). Therefore, for hotter (faster rotating) stars, frequency splitting due to differential rotation might be more easily observed and disentangled from line profile broadening due to the nonstationary nature of

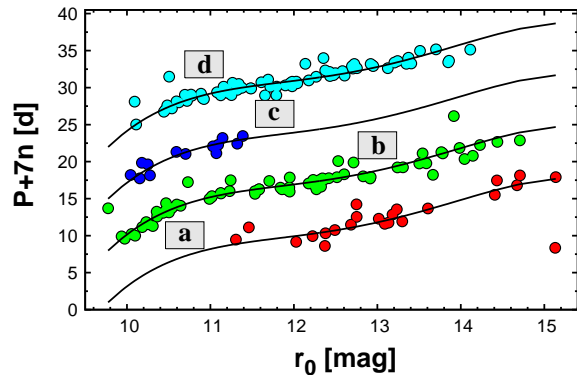


Figure 8. Rotational variables plotted in the dereddened Sloan r magnitude – period plane and separated according to the classification presented in Sect. 3.3. For better visibility, the various classes are shifted by 7 days in the vertical directions (with type (a) left at the original periods).

the spots. On the other hand, the observed frequency spacings do not increase with the luminosity as one might expect from the result of Kitchatinov & Olemskoy (2012).

Finally, for a more direct inspection of the rotational variables, we display some mid-SNR LCs in Fig. 9. It is seen that non-sinusoidal variations are quite common and the LCs are diverse as expected from different geometrical and spot configurations.

4 DO CLOSE-IN PLANETS SPIN UP THEIR HOST STARS?

For close-in planets it is an important question if tidal interaction has any influence on the dynamics of the system, including the rotation of the star. For individual systems in the field it is often difficult to study this question, since most of the parameters (e.g., age, rotational period) necessary to make any reasonably solid statement on this interaction, are among the least accurately determined quantities for single free-floating stars.

With the discovery of the first HJs in Praesepe and Hyades (Quinn et al. 2012, 2014) and quite recently also in M67 (Brucalassi et al. 2014), and the first transiting planets in NGC 6811 (Meibom et al. 2011) it has become possible for the first time to use well-established cluster ages and relative rotational rates to study if planets have any systematic effects on the rotation of their host stars. Although the sample is still fairly small (8 planets, discarding the ones with orbital periods longer than 20 days), we may attempt to examine the relative positions of the planet hosts of these systems on the corresponding color–period diagrams, and see if they show any systematic differences relative to the single (supposedly no giant planet host) stars. Unfortunately, M67 is relatively old, and there are not enough published rotational periods available (e.g., Canto Martins et al. 2011; Stassun et al. 2002). The two TEPs in NGC 6811 have longer periods, and most probably lower masses (in the range of Neptune), therefore, they are probably less relevant in the context of star-planet interaction. Fortunately,

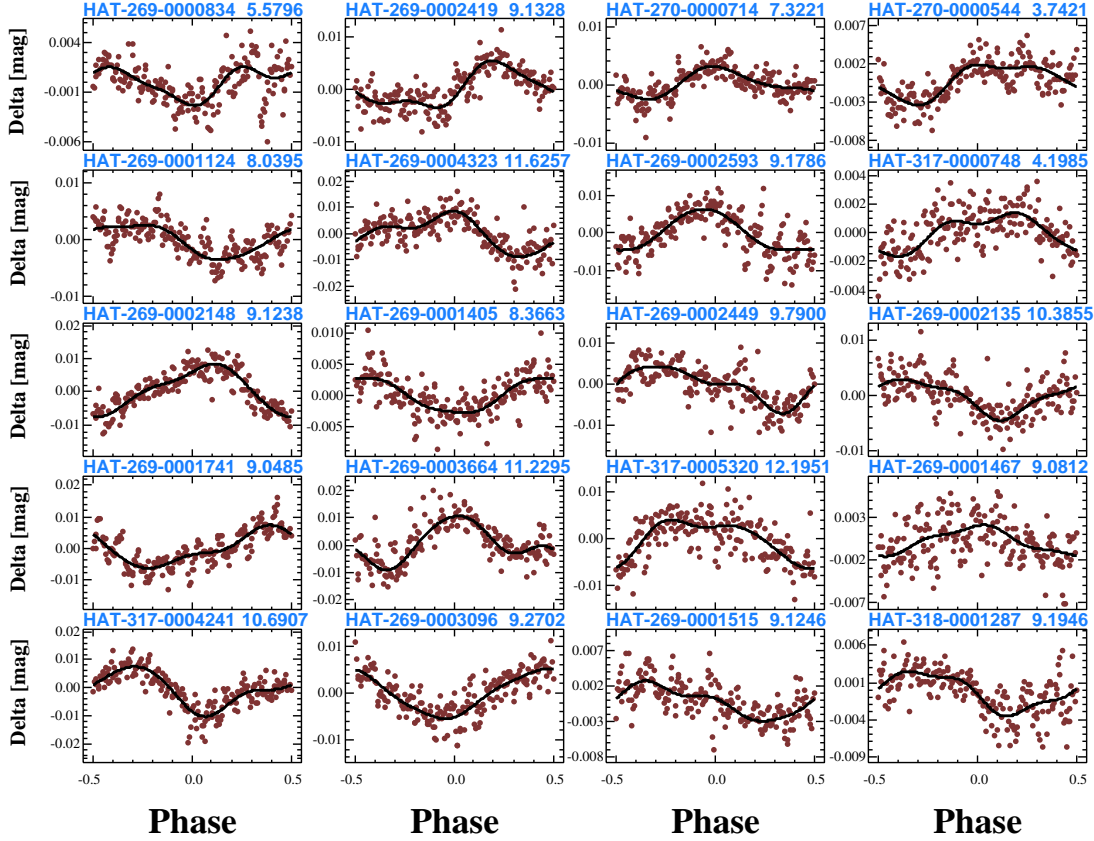


Figure 9. Example of the mid-SNR light curves from the 180 rotational variables. For better visibility, the light curves are binned in 200 bins. The corresponding 3rd-order Fourier fits are shown by continuous lines. The folding period is equal to the rotational period (see Table 2) and shown (in [days]) in the upper right corner of each panel. For this plot we use the original (i.e., EPD, non-TFA-filtered) data. As a result, some of the light curves may contain substantial amount of systematics (e.g., HAT-269-0000834). Phase zero corresponds to HJD 2456000.0 .

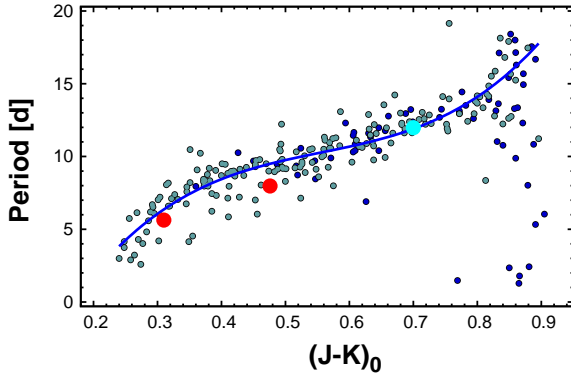


Figure 10. Period– $(J-K)_0$ plot for Praesepe (light filled circles, this paper) and for the Hyades (dark filled circles, Delorme et al. 2011). The RV planets (Quinn et al. 2012, 2014) are shown by the larger filled circles; darker shade for Praesepe and lighter one for Hyades. For reference, the 3rd order polynomial fit to the Praesepe data is also shown.

the remaining three planets in Praesepe and Hyades have photometrically determined rotational rates, as do many of their cluster-mates.

We show the three RV planets together with other known rotational variables on the $(J-K) - \text{period}$ plane in Fig. 10. The rotational rates in the two clusters nicely follow the same pattern in the overlapping region of the main rotational ridge. This further confirms that the two clusters have the same age (Delorme et al. 2011). All three planet hosts are fairly close to the main ridge but the two in Praesepe may be slightly below it. When comparing with a similar plot for the Sloan r color (Fig. 4) we see that although the overall topology is the same, there are differences, attributed in part to the various noise properties of Sloan magnitudes and 2MASS color indices.

We tested various color combinations and appropriate transformations to stellar mass and temperature. They all gave very similar topology, albeit with different scatters. The status of both the cooler (Pr0211=HAT-269-0002316, $P_{\text{orb}} = 2.15$ d, $P_{\text{rot}} = 7.97$ d) and the hotter (Pr0201=HAT-269-0000805, $P_{\text{orb}} = 4.43$ d, $P_{\text{rot}} = 5.63$ d) planet hosts remained basically the same: the hotter one was always closer to (and likely to be on) the ridge, whereas the cooler one retained its relatively distinct position from the ridge. The planet host in the Hyades was also always close to the ridge but usually slightly on the short period side. When checking a similar plot of Meibom et al. (2011) for NGC 6811 (their Fig. 1b), we see that the two planet hosts have also slightly shorter periods than most of the stars at the same colors.

As far as Pr0211, the cooler planet host in Praesepe, is concerned, we find that the distance from the cubic polynomial fit to the ridge (see Sect. 3 and Table 3) varies between -1.96 and -1.62 days, depending on the color combination used.⁸ Although Pr0211 is certainly not the only one with similar deviations, the values quoted correspond nearly 20% difference in rotational rate relative to ‘single normal’ stars, which we consider interesting enough to consider a possible relation between the faster rotation and the planet-hosting status.

If the cause of this difference is the angular momentum exchange between the planet and the host star, then from the models of Brown et al. (2011) we expect this system to be near (within a few hundred million years) to the end of its life time. Unfortunately, the implied decrease of the orbital period would still be under a small fraction of a second over a year, so it is not easy to verify this hypothesis by direct observations. On the other hand, the fact that the two other planet hosts, Pr0201 in Praesepe and HD 285507 in the Hyades sit closer to the respective ridge lines is in agreement with the expectation that in the case of these longer period systems the tidal interaction becomes far less important, and change their rotational periods with the same pace as other, ‘normal’ single stars.

The migration of HJs and their interaction with their host stars is obviously a very complex problem. This complexity is highlighted by the recent result of McQuillan, Mazeh & Aigrain (2013), who, based on the rotational analysis of 737 planet host stars in the Kepler field, showed that fast rotation and short period planet hosting is a low probability event (see also Walkowicz & Basri 2013 and for a possible theoretical explanation Teitler & König 2014). We note however, that there are several/many HJ host stars in the field that rotate fast. For example (just selecting a few representative cases), from the published $V_{\text{rot}} \sin i$ and R_{star} values one can easily derive that WASP-33 and KELT-1 are deeply within the ‘prohibited’ lower left corner of the $P_{\text{orb}} - P_{\text{rot}}$ plot (see Fig. 2 of McQuillan, Mazeh & Aigrain 2013). The evolutionary ages are 0.4 ± 0.30 and 1.75 ± 0.25 Gyr, respectively. The age for WASP-33 is in agreement with the expected gyro age but for KELT-1 the gyro age is shorter by several factors. This indicates that KELT-1 rotates faster than expected for a single star with the same physical parameters. Other hosts, such as WASP-103, HAT-P-32, HAT-P-41, among others, are definitely below the border line of the $P_{\text{orb}} - P_{\text{rot}}$ diagram, and, again, with multiple factors lower gyro ages as expected from the reasonably accurate evolutionary ages. These differences are large, even if we consider that there is a general inconsistency between the gyro and isochrone ages (e.g., Barnes 2009). The two hosts in Praesepe are at the border line, whereas the one in the Hyades is among the many other KOIs in the middle part of the diagram.

⁸ For comparison, Pr0201 yields values between 0.38 and -0.76 days – the latter one is obtained when $J - K$ is used, and also becomes more negative if we use the higher frequency component as the rotational frequency. (Pr0201 has two closely spaced frequency components, corresponding to the periods of 5.63 and 5.19 days.)

5 CONCLUSIONS

We analyzed 381 high probability members of the galactic open cluster Praesepe and found that 47% of them show significant variability, best understood as a consequence of the cyclic variation of the spotted area of the stars due to rotation. We found a fairly tight color/magnitude – period relation, in consonance with the earlier work of Delorme et al. (2011), based on a sample size less than a third of the one presented here. Our sample extends to the lower-amplitude variables at the hotter side, up to early F stars. This, and the dense coverage down to the late K regime, allows us to trace the nonlinearity in the color dependence of the rotational periods. Because of the high-rate sampling and wide color range covered by these data and because of the relatively accurate age of Praesepe, the derived color-period relation is well-suited for gyrochronological age determination (i.e., Skumanich 1972 and Barnes 2003).

We found a rather small number (13%) of the rotational variables with coherent light variation; most of them (39%) have residual power at the main rotational component and there are also many (41%) that have harmonic components. A relatively small fraction (7%) of them show separate but closely spaced frequency components, probably related to differential rotation. This latter type of variables are at the hotter, luminous end of the rotational sequence, whereas the ones with coherent single-period component are found preferably at the cooler (mid/low-luminosity) side. Each type of the other variables (the ones with unstable single component and those with harmonic components) cover uniformly the full color/magnitude range of rotational variables. The amplitudes show a broad range throughout the full span of color. An overall amplitude increase toward redder/fainter colors/magnitudes is also observable. However, this increase is largely attributed to the higher detection limits for those fainter stars.

From the two planet hosting stars the cooler one (Pr0211) has a rotational period that is ~ 2 days shorter than the one predicted by the main rotational relation at the given color in this cluster. Although there are several other – supposedly not planet host – stars with similar deviations, we may interpret this shorter period as a possible result of the exchange of angular momentum between the star and the planet at the expense of the planet’s orbital angular momentum. This inference is perhaps corroborated by the fact that the other planet (and also HD 285507 in the Hyades) are much closer to the corresponding ridge values. The planets in these systems have 2 – 3-times longer orbital periods than the one in Pr0211, so we expect considerably weaker tidal interactions. Also, as discussed in Sect. 4, there are several Hot Jupiter planet hosts in the field that rotate faster than expected from their isochrone ages. The host of Pr0211 b could be one of these spun-up stars.

ACKNOWLEDGMENTS

We thank the referee Aleks Scholz for the valuable comments that helped to improve the paper. This publication makes use of data products from the Two Micron All Sky Survey, which is a joint project of the University of Massachusetts and the Infrared Processing and Analysis Cen-

ter/California Institute of Technology, funded by the National Aeronautics and Space Administration and the National Science Foundation. This research was made possible through the use of the AAVSO Photometric All-Sky Survey (APASS), funded by the Robert Martin Ayers Sciences Fund, the SIMBAD database and the VizieR catalogue access tool, operated at CDS, Strasbourg, France. G. K. thanks the Hungarian Scientific Research Foundation (OTKA) for support through grant K-81373. HATNet observations have been funded by NASA grants NNG04GN74G and NNX13AJ15G. G.Á. B., Z. C. and K. P. acknowledge partial support from NASA grant NNX09AB29G. J. H. acknowledges partial support from NSF grant AST-1108686 and NASA grant NNX14AF87G. K.P. acknowledges support from NASA grant NNX13AQ62G. S. Q. acknowledges support from NSF grant DGE-1051030.

REFERENCES

- Agüeros, Marcel A. et al., 2011, *ApJ*, 740, 110
 Bakos G. A. et al., 2004, *PASP*, 116, 266
 Bakos G. Á. et al., 2010, *ApJ*, 710, 1724
 Balona, L. A., Joshi, S., Joshi, Y. C., Sagar, R., 2013, *MNRAS*, 429, 1466
 Barnes, S. A., 2003, *ApJ*, 586, 464
 Barnes, S. A., 2009, *IAUS*, 258, 345
 Boesgaard A. M., Roper B. B., 2013, *ApJ*, 775, 58
 Breger M. et al., 2012, *AN*, 333, 131
 Bressan, A. et al., 2012, *MNRAS*, 427, 127
 Brown D. J. A., Collier Cameron A., Hall C., Hebb L., Smalley, B., 2011, *MNRAS*, 415, 605
 Brucalassi A. et al., 2014, *A&A*, 561, L9
 Bouvier J. et al., 2013, *arXiv1309.7851*
 Canto Martins B. L. et al., 2011, *A&A*, 527, 94
 Cargile P. A., 2013, *ApJ*, in press, *arXiv1312.3946*
 Collier Cameron A. et al., 2009, *MNRAS*, 400, 451
 Deeming, T. J., 1975, *Ap&SS*, 36, 137
 Dékány I., Kovács G., 2009, *A&A*, 507, 803
 Delorme P. et al., 2011, *MNRAS*, 413, 2218
 Fossati L. et al., 2008, *A&A*, 483, 891
 Franciosini E., Randich S., Pallavicini R., 2003, *AdSpR*, 32, 1143
 Gaspar A. et al., 2009, *ApJ*, 697, 1578
 Hartman J. D. et al., 2009, *ApJ*, 691, 342
 Hartman J. D., Bakos G. A., Kovács G., Noyes R. W., 2010, *MNRAS*, 408, 475
 Irwin J. et al., 2009, *MNRAS*, 392, 1456
 Khalaj P., Baumgardt H., 2013, *MNRAS*, 434, 3236
 Kitchatinov L. L., Olemskoy S. V., 2012, *MNRAS*, 423, 3344
 Kovács G., Bakos G. Á. Noyes, R. W., 2005, *MNRAS*, 356, 557
 Kraus A. L., Hillenbrand L. A., 2007, *AJ*, 134, 2340
 Lovis C., Mayor M., 2007, *A&A*, 472, 657
 Mamajek, Eric E., Hillenbrand, Lynne A., 2008, *ApJ*, 687, 1264
 McQuillan A., Aigrain S., Mazeh T., 2013, *MNRAS*, 432, 1203
 McQuillan A., Mazeh T., Aigrain S., 2013, *ApJ*, 775, L11
 Meibom, S. et al., 2011, *ApJ*, 733, L9
 Meibom S. et al., 2013, *Nature*, 499, 55
 Mermilliod J.-C., Duquennoy A., Mayor M., 1994, *A&A*, 283, 515
 Mermilliod J.-C., Mayor M., Udry S., 2009, *A&A*, 498, 949
 Messina S., Guinan E. F., 2002, *A&A*, 393, 225
 Noyes R. W., Hartmann L. W., Baliunas S. L., Duncan D. K., Vaughan A. H., 1984, *ApJ*, 279, 763
 Penev K., Jackson, B., Spada, F., Thom, N., 2012, *ApJ*, 751, 96
 Pepper J. et al., 2008, *AJ*, 135, 907
 Quinn S. N. et al., 2012, *ApJ*, 756, L33
 Quinn S. N. et al., 2014, *ApJ*, 787, 27
 Saar S. H., Dyke M., Meibom S., Barnes S. A., 2011, *IAUS*, 273, 469
 Sato B. et al., 2007, *ApJ*, 661, 527
 Scholz A., Eislöffel J., 2007, *MNRAS*, 381, 1638
 Scholz A. et al., 2011, *MNRAS*, 413, 2595
 Skumanich A., 1972, *ApJ*, 171, 565
 Stetson P. B., 2000, *PASP*, 112, 925
 Stassun K. G., van den Berg M., Mathieu R. D., Verbunt F., 2002, *A&A*, 382, 899
 Szulágyi J., Kovács G., Welch D. L., 2009, *A&A*, 500, 917
 Taylor B. J., 2006, *AJ*, 132, 2453
 Teitler S., Knigl A., 2014, *ApJ*, in press, *arXiv1403.5860*
 Yuan H. B., Liu X. W., Xiang, M. S., 2013, *MNRAS*, 430, 2188
 van Leeuwen F., 2009, *A&A*, 497, 209
 Walkowicz L. M., Basri, G. S., 2013, *MNRAS*, 436, 1883
 Wang, P. F. et al., 2014, *ApJ*, 784, 57
 Zhang M., Penev, K., 2014, *arXiv:1404.4365v2* (submitted to *ApJ*)

APPENDIX A: NON-ROTATIONAL VARIABLES

By following the methodology employed in the search for rotational variables, we searched for other types of variables among the 381 high-probability cluster members (see Sect. 2.1). We found 10 variables in the frequency range of $[0,50]d^{-1}$. Table A1 displays the most important properties of these variables. Figures A1 and A2 show the frequency spectra and the folded light curves for variables with frequencies greater than $1d^{-1}$. The case of HAT-269-0000465 is special. It is KW 495, a triple spectroscopic system (Mermilliod et al. 1994). Its frequency spectrum is rather complicated with two main frequency clumps at ~ 0.079 and $\sim 0.207d^{-1}$. The data are insufficient to classify this variable. Because of the detected period range, it is possible that the source of the signal is the rotation of two of the member stars. Alternatively, the complicated frequency spectrum and the late F (or early G) spectral type may suggest that this is a γ Dor-type star.

In a technical note we mention that in several cases the application of TFA filtering was necessary for an unambiguous detection. Since the time series are the result of the merging of the data from the individual fields, and our main interest is to detect variability, we do not employ signal reconstruction as the second phase in the TFA filtering process (see Kovács et al. 2005). As a result, except for HAT-269-0000582, where the signal was stronger in the data before TFA filtering, the amplitudes are lower in the panels of Fig-

ures A1, than the ones listed in Table A1, where we used the original (EPD) data to compute the total amplitudes.

Most of the variables are known and classified as of δ Scuti type. We have probably 3 new discoveries (i.e., none of them are listed in the site of CDS nor mentioned in the current literature summary of this site on Praesepe). Star HAT-269-0000277 is most likely a pulsating variable with closely-spaced frequency components. This, together with the shape of the light curve, strongly suggests that this variable is a nonradial pulsator. The other object (HAT-270-0000165) is clearly a δ Scuti star.

It is interesting to compare the frequencies we obtained with those of Breger et al. (2012) derived from the data observed by the MOST satellite for the two variables common in these two studies. For BS Cnc Breger et al. (2012) detected 20 frequencies. We have good agreement for the main component: $(\nu_0, \text{Amp}) = (17.0363, 0.0062)$ for MOST and $(17.03626, 0.0068)$ for HATNet (please note that our amplitude corresponds to the total signal amplitude - including also the [small] contribution of the other signal components). We also detected another component at 31.60299 d^{-1} with a much lower significance, at an amplitude nearly a third that of the main component. Interestingly, among the 20 components they found in the MOST data, there is the 10th component with basically the same frequency: $f_{10} = 31.5988$. Breger et al. (2012) mention the puzzling nature of this component, since it was actually absent in their 2008 dataset whereas had a relatively large amplitude of 2.1 mmag in 2009. Our data cover the period of December 2008 and June 2011 (with a large gap between May 2009 and November 2011). Therefore, it is likely that the amplitude of this component was still significant after 2009.

The variability of HD 73872 was discovered by the MOST satellite. Some 18 components were detected, with the main component at $(\nu_0, \text{Amp}) = (33.416, 0.0030)$ and a second one at $(35.981, 0.0025)$. We found a significant component at 33.41569 d^{-1} and a far less significant one as the second component at 34.97772 d^{-1} . This latter one is very close to the 1 d^{-1} alias of the second component listed by Breger et al. (2012).

APPENDIX B: SPECTROSCOPIC BINARIES

The status of the spectroscopic binaries (SBs) associated with the cluster has been summarized recently by Mermilliod et al. (2009). Based on their data collected by the CORAVEL spectrograph over a period of nearly two decades, they presented the orbital elements of 29 SBs. When we cross-correlate these stars with the 381 stars selected from the overlap of the list of cluster members given by Kraus & Hillenbrand (2007) and the HATNet database, we get a list of 24 stars. The spectroscopic (orbital) and photometric frequencies of these objects are shown in Table B1. The photometric frequency is the one that corresponds to the highest peak in the spectrum and does not necessarily agree with the finally adopted rotational frequency (see Table 2 for comparison). As discussed in the Sect. 6.1, the variable type of HAT-269-0000465 is unclear in spite of its high SNR.

We see that the orbital periods are, in general, much longer than the rotational periods. There are only three

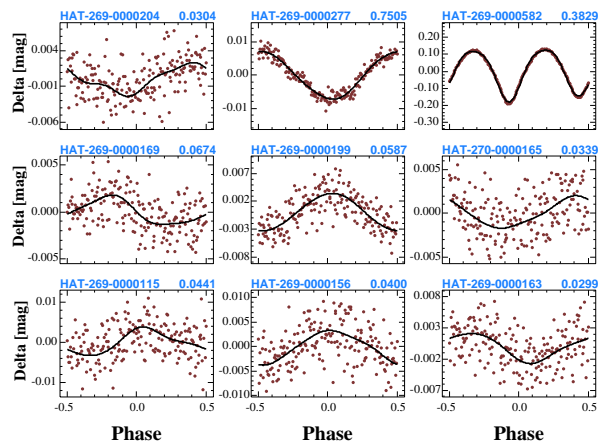


Figure A2. Folded light curves of the non-rotational variables found in the analysis of the 381 Praesepe members with periods shorter than 1 day. For better visibility the folded data are binned in 200 bins. The continuous line is the 3-rd (for HAT-269-0000582 the 5-th) order Fourier fit. The relatively large scatter in some cases is due to in part of the multiperiodic nature of these, mostly δ Scuti-type variables. Except for the upper two panels, the total amplitudes are smaller than those given in Table A1, since we used the TFA-filtered light curves without the reconstructive option.

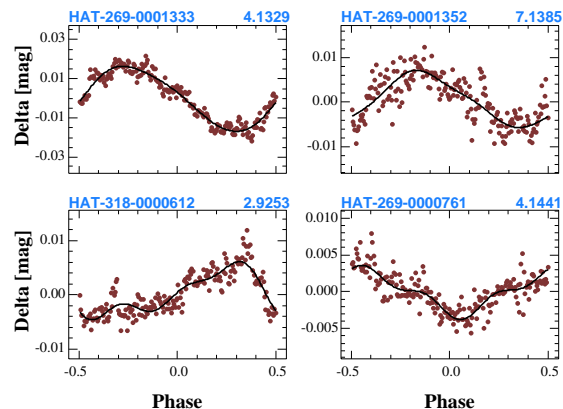


Figure A3. Folded light curves of the four rotational variables that have close periods to the spectroscopic periods given by Mermilliod et al. (2009). For better visibility the data are binned in 200 bins. The continuous line is the 3-rd order Fourier fit. The original (EPD) data are used, without TFA filtering.

cases when we might face some ambiguity in distinguishing between the light variations caused by eclipses and by spots. However, inspecting the folded light curves does not lend too much support to the eclipse hypothesis, since they all seem to have distorted sinusoidal shape, with no resemblance of an eclipsing binary (see Figure A3). There is a fourth variable (HAT-269-0000761), which is an outlier in the color-period diagram with orbital and rotational periods differing by some 30%. We could not find any trace of the orbital period in the photometric data. However, when we compare the photometric frequency with the one computed

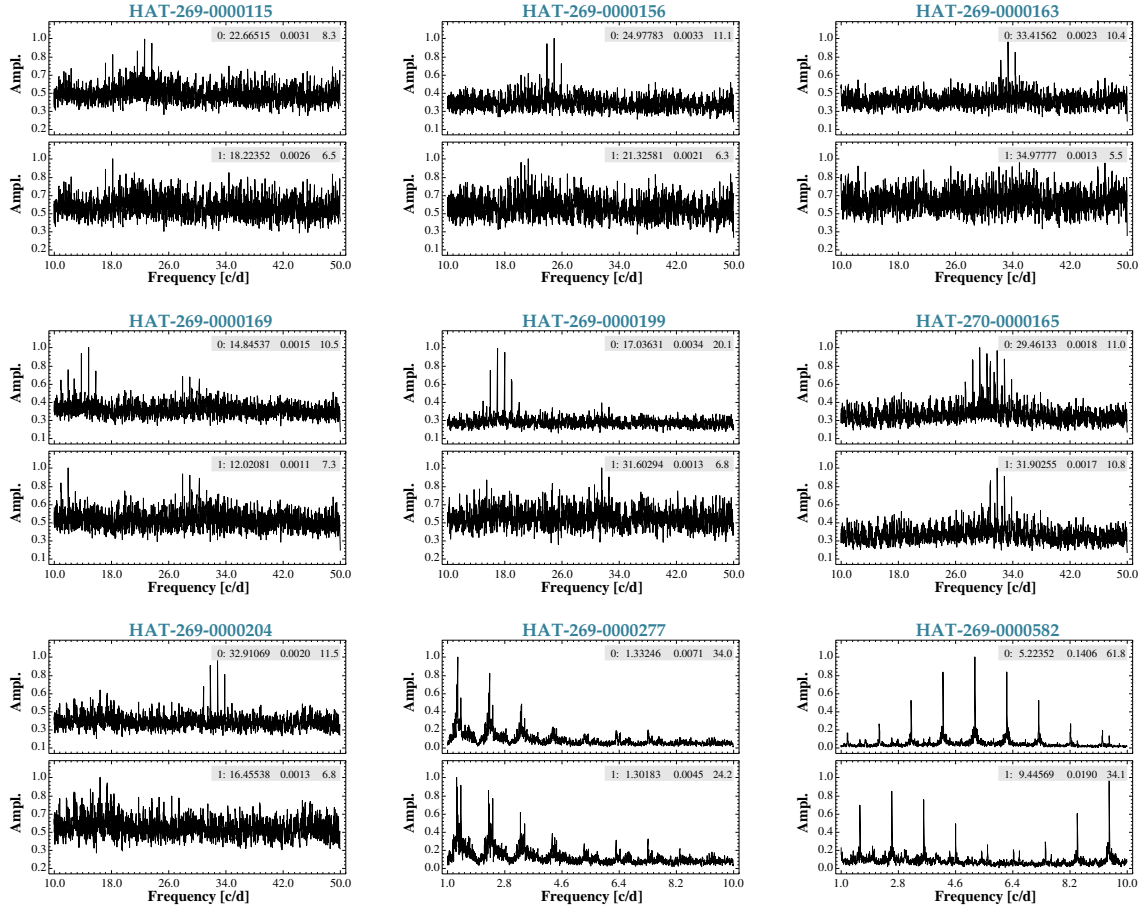


Figure A1. Frequency spectra of the non-rotational variables with frequencies higher than 1 d^{-1} . In each sub-figure the upper and lower panels show, respectively, the frequency spectra of the data and the spectra obtained after the first pre-whitening (with the peak frequency shown on the upper panel). The insets show the pre-whitening order, the peak frequency, the amplitude and the SNR of the peak.

from the rotational velocity of 11.9 kms^{-1} (Mermilliod et al. 2009), we get $f_{\text{rot}} = 0.2547 \text{ d}^{-1}$ (see Sect. 3.1 for details of the estimation of the necessary physical parameters of the star). This is in a very nice agreement with our photometric frequency.

Table A1. Non-rotational variables in Praesepe detected in the HATNet database

HAT ID	2MASS ID	Other ID	ν [d ⁻¹]	K [mag]	J-K [mag]	A [mag]	SNR	Type
HAT-269-0000115	08420650+1924405	BX Cnc	22.6652144	7.431	0.114	0.0072	8.3	δ Scuti
HAT-269-0000156	08374070+1931063	BR Cnc	24.9778239	7.662	0.117	0.0078	11.1	δ Scuti
HAT-269-0000163	08411377+1955191	HD 73872	33.4156874	7.774	0.101	0.0054	10.4	δ Scuti
HAT-269-0000169	08405247+2015594	BW Cnc	14.8453080	7.804	0.107	0.0036	10.5	δ Scuti
HAT-269-0000199	08390909+1935327	BS Cnc	17.0362610	7.875	0.131	0.0068	20.1	δ Scuti
HAT-270-0000165	08452825+2023435	HD 74587	29.4613325	7.864	0.148	0.0039	11.0	δ Scuti
HAT-269-0000204	08403296+1911395	BV Cnc	32.9106985	7.964	0.119	0.0047	11.5	δ Scuti
HAT-269-0000277	08411067+1949465	HD 73854	1.3324437	8.190	0.174	0.0148	34.0	puls.?
HAT-269-0000465	08430593+1926152	BD+19 2087	0.2071673	8.461	0.333	0.0050	20.8	misc.?
HAT-269-0000582	08400171+1859595	TX Cnc	5.2235226	8.698	0.355	0.2983	61.8	EB

Notes: For variables with peak frequency $1 < \nu < 10$ [d⁻¹] the signal-to-noise ratio (SNR) is computed in the [1, 10] d⁻¹ band. For those with $\nu > 10$ [d⁻¹], the [10, 50] d⁻¹ band is used. Amplitudes A [mag] are peak-to-peak values from the 4th order Fourier fit to the instrumental Sloan “r” light curves, without TFA filtering. For the special case of HAT-269-0000465 the amplitude is a rough visual estimate of the total range of variation. For other details of this object, see text.

Table B1. Spectroscopic binaries in Praesepe

HAT ID	KW ID	K	J-K	f_{phot}	f_{orb}	$f_{\text{orb}}/f_{\text{phot}}$	SNR
HAT-269-0000913	508	7.293	0.300	0.16167	0.00154	0.0095	22.9
HAT-269-0000528	47	7.353	0.338	6.28626	0.02889	0.0046	5.2
HAT-269-0000761	181	7.431	0.360	0.24131	0.17047	0.7064	23.1
HAT-269-0000489	268	7.610	0.259	0.58068	0.00693	0.0119	5.4
HAT-269-0000396	416	7.637	0.217	1.37448	0.03870	0.0282	5.0
HAT-269-0000726	3532	7.662	0.358	1.11693	0.02944	0.0264	3.5
HAT-269-0000465	495	7.769	0.333	0.21501	0.02786	0.1296	17.8
HAT-269-0000598	549	7.774	0.262	4.17972	0.03196	0.0076	5.9
HAT-269-0001333	434	7.790	0.383	0.24196	0.25428	1.0509	38.4
HAT-318-0000612	3655	7.804	0.422	0.34184	0.33537	0.9811	23.7
HAT-269-0001352	55	7.864	0.535	0.14009	0.16708	1.1927	22.0
HAT-269-0000767	287	7.875	0.363	1.45366	0.00014	0.0001	4.8
HAT-269-0000556	365	7.944	0.359	0.12007	0.01952	0.1626	7.2
HAT-269-0001570	368	7.946	0.430	0.11103	0.01306	0.1176	10.9
HAT-269-0000850	325	7.964	0.396	0.32065	0.00346	0.0108	8.5
HAT-269-0000287	142	8.044	0.241	0.37165	0.02175	0.0585	4.9
HAT-269-0000372	439	8.051	0.207	8.88541	0.00218	0.0002	4.8
HAT-269-0001402	539	8.063	0.396	0.26847	0.00018	0.0007	20.8
HAT-269-0000968	127	8.100	0.329	0.90909	0.07530	0.0828	6.2
HAT-269-0007340	536	8.190	0.873	0.58212	0.00079	0.0014	5.2
HAT-269-0000794	556	8.221	0.366	0.22052	0.00700	0.0317	26.2
HAT-269-0001490	184	8.351	0.502	0.09536	0.02108	0.2211	13.0
HAT-317-0001780	2025	8.369	0.503	0.20720	0.00038	0.0018	18.6
HAT-269-0003949	1184	8.377	0.660	9.57013	0.81290	0.0849	3.7

Notes: Photometric (f_{phot}) and orbital (f_{orb}) frequencies (in [d⁻¹]), respectively, are taken from this paper and from Mermilliod et al. (2009). The signal-to-noise ratio (SNR) refers to the peak frequency in the [0, 10]d⁻¹ band, and is computed from the Fourier spectra of the TFA-filtered data. See text for more about f_{phot} and on the status of HAT-269-0000465.